

Numerical study for downburst wind and its load on high-rise building

Guoqing Huang^{1,2a}, Weizhan Liu^{1b}, Qiang Zhou^{*1}, Zhitao Yan^{2c} and Delong Zuo^{3d}

¹School of Civil Engineering, Southwest Jiaotong University, Chengdu, Sichuan, 610031, China

²School of Civil Engineering, Chongqing University, Chongqing, 400044, China

³Department of Civil, Environmental and Construction Engineering, Texas Tech University, Lubbock, TX 79409, USA

(Received March 8, 2018, Revised June 21, 2018, Accepted June 29, 2018)

Abstract. 3D simulations based on an impinging jet were carried out to investigate the flow field of a steady downburst and its effects on a high-rise building by applying the SST $k-\omega$ turbulence model. The vertical profile of radial wind speed obtained from the simulation was compared with experimental data and empirical models in order to validate the accuracy of the present numerical method. Then wind profiles and the influence of jet velocity and jet height were investigated. Focusing on a high-rise building, the flow structures around the building, pressure distributions on the building surfaces and aerodynamic forces were analyzed in order to enhance the understanding of wind load characteristics on a high-rise building immersed in a downburst.

Keywords: downburst; numerical study; impinging jet; high-rise building; flow structure; pressure distribution; aerodynamic force

1. Introduction

The extreme climate events induced by non-synoptic winds, such as tornados and downbursts, are responsible for damages of many structures such as transmission lines and buildings around the world (e.g., Holmes 1999, Aboshosha *et al.* 2016, Yang 2018). However, the current wind-resistant design methods and codes are based on synoptic winds. Therefore, in order to ensure the safety and comfort of wind-sensitive structures, it is quite essential to study the flow field of a downburst and its effects on high-rise buildings, which has also been one of the most attractive and frontier issues in wind engineering.

A downburst is an intense downdraft air that induces an outburst of damaging wind when striking the ground (Fujita 1985). Characterizing and modeling these extreme winds and their effects on structures have drawn significant attention from meteorological and wind engineering communities (e.g., Holmes and Oliver 2000, Huang *et al.* 2015, Solari *et al.* 2015, Peng *et al.* 2018). Although it is difficult to capture downbursts in the field due to small temporal and spatial scales, and random occurrences, limited full-scale measurements were obtained by Fujita (1985), Gast and Schroeder (2003), Lombardo *et al.* (2014)

and De Gaetano *et al.* (2014).

Compared with limited field measurements on downburst, more work has been performed by physical and numerical simulations. Chay and Letchford (2002) carried out physical experiments to study the characteristics of pressure distributions on a cube immersed in a stationary downburst. Choi (2004) carried out experimental studies on the simulation of thunderstorm wind using a steady impinging jet to investigate the effect of distance from the thunderstorm center and ground roughness on the wind profiles. Butler *et al.* (2010) investigated the surface pressure and wind load characteristics on prisms immersed in a simulated transient gust front flow field generated by a multiple fan wind tunnel. Zhang *et al.* (2014) investigated the wind loads of a downburst acting on a high-rise building with different positions. Zhang *et al.* (2014) also mentioned that it is possible and reasonable for a steady-state impinging jet model to simulate the main features of a downburst, though the downburst usually occurs within a duration of about 10 minutes.

On the other hand, the numerical approach is widely used as the result of the rapidly developing computing ability. Selvam and Holmes (1992) used a two dimensional $k-\epsilon$ model to simulate impingement of a steady jet of air on a ground plane. Kim and Hangan (2007) studied the relationship between the flow field and Reynolds number with the Reynolds stress model at $Re = 2 \times 10^4$, 1×10^5 and 2×10^6 , respectively. Sengupta and Sarkar (2008) simulated the downburst wind field by using a variety of turbulence models and compared the numerical results with the experimental results to explore the optimal turbulence model, boundary conditions and computational domain for the downburst numerical simulation. Mason *et al.* (2009) simulated the stationary downburst wind storm using an axisymmetric, dry, non-hydrostatic cooling source method. Sim *et al.* (2016) conducted a numerical investigation on

*Corresponding author, Ph.D. Lecturer

E-mail: milan1023@gmail.com

^a Professor

E-mail: ghuang1001@gmail.com

^b Graduate Student

E-mail: vamswjtu@163.com

^c Professor

E-mail: yanzhitao@cqu.edu.cn

^d Professor

E-mail: delong.zuo@ttu.edu

the microburst-like wind characteristics in block array configurations using an impinging jet.

As mentioned above, most of the numerical studies were carried out on the wind field structure of a downburst. Less attention has been devoted to the effects of downburst on a high-rise building, which is important and essential for structural wind engineering. In the present study, a steady 3D downburst and its effects on a high-rise building are investigated by using a *RANS SST k- ω* model. First, a steady impinging jet model is used to numerically simulate a steady downburst, which is validated by the wind velocity profile. Afterwards, more focus is directed towards the investigation of wind profiles, as well as the effect of jet velocity and jet height on the downburst characteristics. Finally, based on a high-rise building, which is used in the experiment by Zhang *et al.* (2014), the flow structures around the building, pressure distributions on the building surfaces and aerodynamic forces are investigated.

2. Numerical simulation

2.1 Governing equations and numerical algorithm

The numerical simulation of the downburst is carried out by using the steady *RANS* method. Continuity equation and momentum equation are given as follows

$$\frac{\partial \rho}{\partial t} + \frac{\partial}{\partial x_i} (\rho u_i) = 0 \quad (1)$$

$$\frac{\partial}{\partial t} (\rho u_i) + \frac{\partial}{\partial x_j} (\rho u_i u_j) = -\frac{\partial p}{\partial x_i} + \frac{\partial}{\partial x_j} \left(\mu \frac{\partial u_i}{\partial x_j} - \overline{\rho u_i u_j} \right) + S_i \quad (2)$$

where ρ is the air density; u_i ($i = 1, 2, 3$) are the three velocity components; p is the pressure; μ is the dynamic viscosity coefficient; $-\overline{\rho u_i u_j}$ is Reynolds stress term, which makes the equations unclosed. So the term $-\overline{\rho u_i u_j}$ needs to be numerically modeled to close the equations. According to the different treatments over the Reynolds stress term, numerous turbulence models have been proposed. The standard *k- ϵ* model is the most representative two-equation model. However, the standard *k- ϵ* model is not particularly ideal for predicting anisotropy turbulence due to the separation and backflow on the lateral and leeward faces of the building. The *SST k- ω* turbulence model combines the advantages of the *k- ω* model in the near-wall region with the advantages of the *k- ϵ* model in the far field (Menter 1992, 1994). The turbulence model *SST k- ω* is chosen in this paper. The modeled *k* and ω equations are given by Fluent (2005).

$$\frac{\partial (\rho k)}{\partial t} + \frac{\partial (\rho k u_i)}{\partial x_i} = \frac{\partial}{\partial x_j} \left[\left(\mu + \frac{\mu_t}{\sigma_k} \right) \frac{\partial k}{\partial x_j} \right] + G_k - Y_k + S_k \quad (3)$$

$$\frac{\partial (\rho \omega)}{\partial t} + \frac{\partial (\rho \omega u_i)}{\partial x_i} = \frac{\partial}{\partial x_j} \left[\left(\mu + \frac{\mu_t}{\sigma_\omega} \right) \frac{\partial \omega}{\partial x_j} \right] + G_\omega + D_\omega - Y_\omega + S_\omega \quad (4)$$

where G_k represents the generation of turbulent kinetic energy k ; G_ω represents the generation of ω ; Y_k and Y_ω represent the dissipations of k and ω due to turbulence, respectively; S_k and S_ω are user-defined source terms; D_ω denotes the cross-diffusion term.

In the present study, second order is used for pressure interpolation. Second order upwind scheme is used for the momentum term, and Quadratic Upstream Interpolation for Convective Kinematics (QUICK) is used for k and ω terms. The Semi Implicit Method for Pressure Linked Equation Consistent (SIMPLEC) algorithm is used for pressure-velocity coupling in the present simulation. Like the Semi Implicit Method for Pressure Linked Equation (SIMPLE) algorithm, the momentum equation is solved with a guessed pressure field in the SIMPLEC algorithm. Hence the resulting face flux does not satisfy the continuity equation and a correction is added to the face flux. Compared with the SIMPLE algorithm, the flux correction method in the SIMPLEC algorithm has been improved to accelerate convergence. Convergence is assumed to be obtained when the variables of the monitoring points reach a steady state.

2.2 Grid system and boundary conditions

Fig. 1 shows the schematic diagram of computational domain. The X -axis and Z -axis correspond to the horizontal direction and vertical direction, respectively. Sengupta and Sarkar (2008) showed that the effects of computational domain size on the downburst profile can be negligible, when the horizontal radius is 10 times larger than the radius of the nozzle and vertical dimension is larger than the jet height. Considering the full development of turbulence and consumption of computing resources simultaneously, the computational domain is $20D$ (length) \times $20D$ (width) \times $6D$ (height) as shown in Fig. 1, which is the same as that in the numerical study of Sengupta and Sarkar (2008), and D is the diameter of the jet nozzle. According to the experiment by Zhang *et al.* (2014), the jet nozzle diameter D is 610 mm. The jet height $H = 2D$ is used in present study. In addition, the high-rise building model with 45 mm (length) \times 45 mm (width) \times 180 mm (height) in the experiment by Zhang *et al.* (2014) is considered herein for the comparative study.

In order to improve the computational efficiency and accuracy, structured grids are adopted in this study as shown in Fig. 2. Near the wall surfaces, the grids should be fine enough to adequately resolve the near-wall flow. The depth of the first cell is characterized by a dimensionless amount of y^+

$$y^+ = \frac{\Delta y}{\nu} \sqrt{\frac{\tau_w}{\rho}} \quad (5)$$

where Δy is the depth of first cell near the wall; ν is the kinetic viscosity; τ_w is the wall shear stress. The depth of the first cell is $\Delta y/D = 5 \times 10^{-4}$, and the maximum y^+ is less

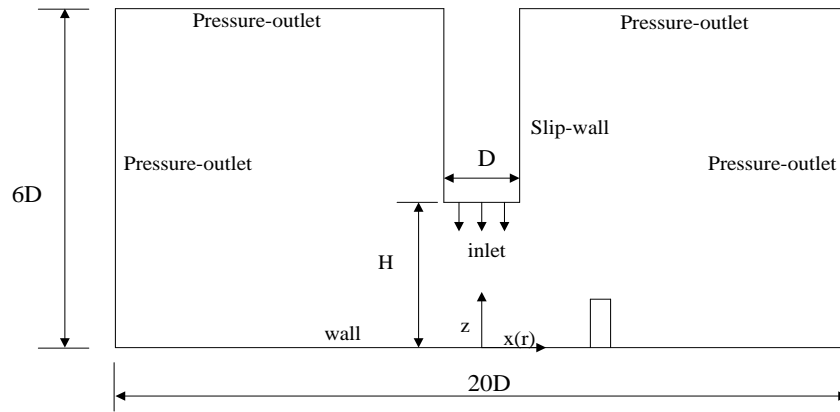
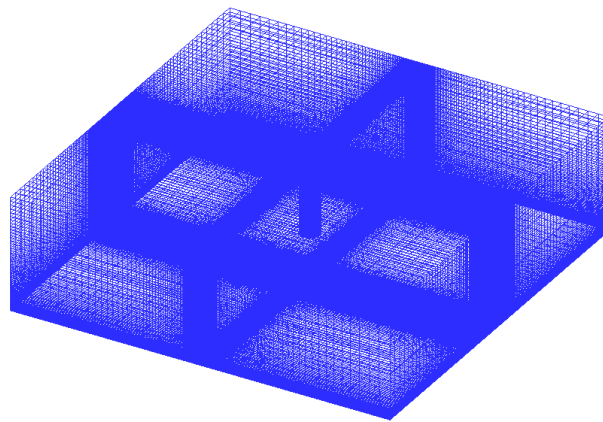
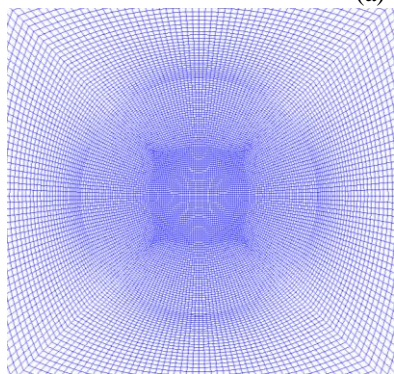


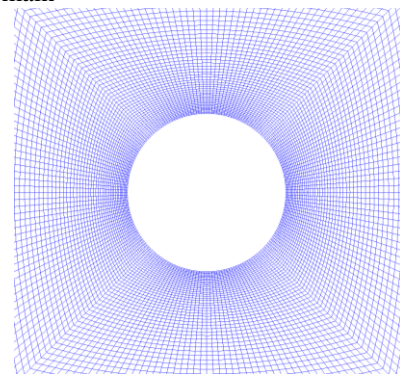
Fig. 1 Schematic diagram of computational domain



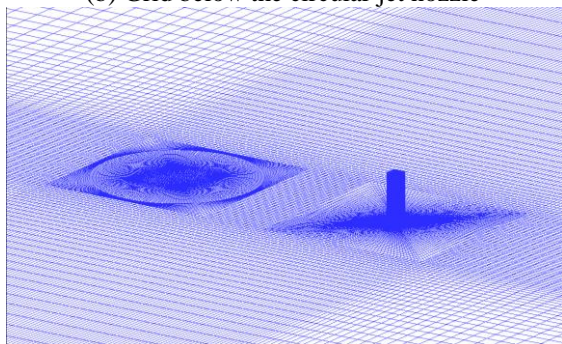
(a) Grid of computational domain



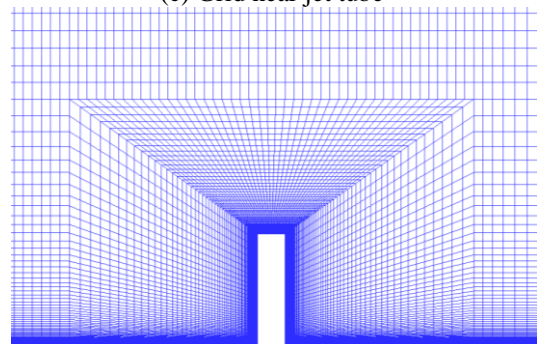
(b) Grid below the circular jet nozzle



(c) Grid near jet tube



(d) Grid on building surfaces and ground surface



(e) Detail of grid near building surfaces

Fig. 2 Grid system

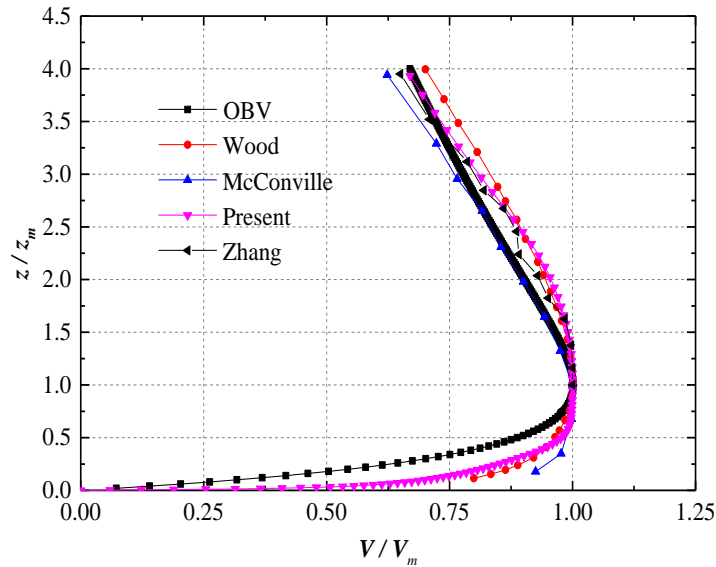


Fig. 3 Comparison of present numerical wind profile with other profiles

than 1. The total number of grid cells is about 6 million. Note that the sensitivity analysis with cell numbers of 6 million, 5 million and 3 million in the beginning of the numerical study is conducted, respectively. Results show that 6 million and 5 million cells agree well.

The boundary conditions for the simulation, as illustrated in Fig. 1, are given hereafter. Inlet: velocity condition, $V_{jet} = 13$ m/s, turbulence intensity = 1%, hydraulic diameter = D . The side and top of the computational domain: pressure-outlet condition, backflow turbulence intensity = 1%, backflow hydraulic diameter = D . Jet surface: a slip wall condition. Building and ground surface: a no-slip condition for $u_i = 0$.

3. Results and discussion

3.1 Comparison of vertical profile of radial wind speed

In order to validate the present simulation, the vertical profile of radial wind speed, a key parameter of the downburst wind field, is compared. Fig. 3 shows the normalized vertical profile of radial wind speed at the position $r = 1.5D$ obtained by present simulation at $Re = 5.3 \times 10^5$. Reynolds number is defined as $Re = V_{jet} D / \nu$, where D is the jet diameter, V_{jet} is the jet velocity and ν is the kinematic viscosity. The radial velocity V is normalized by the maximum radial velocity V_m , and the vertical height z is normalized by the height z_m where the maximum radial wind speed occurs. In addition, the empirical models of OBV (Vicroy 1991), Wood (Wood *et al.* 2001), as well as the physical test results from McConville *et al.* (2009) based on impinging jet model ($r = 1.5D$, $H = 2D$, $Re = 1.05 \times 10^6$) and Zhang *et al.* (2014) are shown for comparison. With the exception of the normalized results, the typical parameters are also given hereafter. As for the max velocity is $V_{max} = 0.99V_{jet}$ obtained by our numerical

simulation, which agrees well with Zhang's experimental result of $V_{max} = 0.96V_{jet}$. As for the corresponding height of the max velocity in present study is $0.032D$ which is consistent with those of previous experiments (e.g., $0.030D$ in the experimental study of McConville *et al.* 2009). It can be seen that the present numerical results are in good agreement with other empirical models and experimental results. It means that the numerical method and the grid system utilized in present simulation for a steady downburst are appropriate. Therefore, they will be used in simulating the wind field of a downburst and its effects on a high-rise building.

3.2 Wind profiles

Fig. 4 shows the vertical profile of radial wind speed at different radial positions, where the radial wind speed V is normalized by the jet velocity at the jet nozzle V_{jet} , and the vertical height z is normalized by the diameter of the nozzle D . It can be found that the numerical simulation well presents the key characteristics of the radial wind speed profiles of downburst. Similar to the previous studies (Chay and Letchford 2002, Xu and Hangan 2008), the radial wind speed rapidly reaches the maximum value near the ground, exhibiting strong shear velocity, then decreases with the increase of height. At $z/D = 0.20$, the radial wind speed remains only 18% -30% of the jet velocity V_{jet} . As is shown in Fig. 4, radial wind speed has not yet developed sufficiently at the radial position $r = 0.75D$. In the radial range of $r = 1.5D - 3.0D$, the radial wind speed decreases as the radial position moves away from downburst center. In contrast to the conventional atmospheric boundary layer wind whose wind speed profile follows an exponential or logarithmic relationship along the height, the maximum velocity of the radial wind in the downburst occurs near ground, showing the nose-shaped characteristics of the wind speed profile.

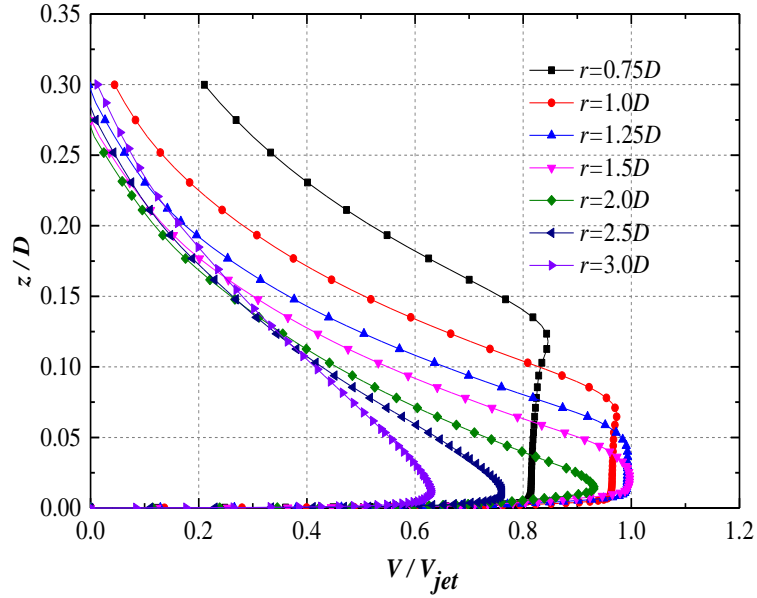


Fig. 4 Vertical profiles of radial wind speeds at different radial positions

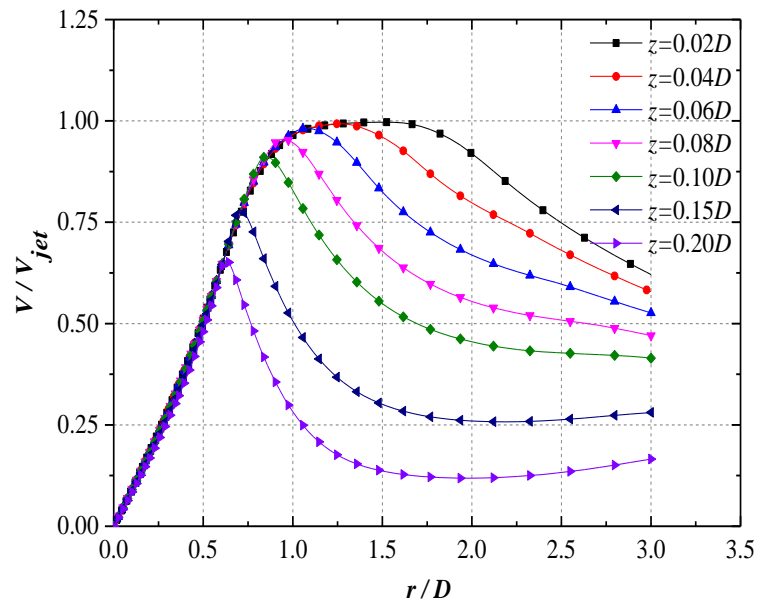


Fig. 5 Horizontal profile of radial wind speed at different heights

Fig. 5 shows the horizontal profile of radial wind speed at different heights. It can be found that the radial wind speed at the center of the downburst is close to zero. As the horizontal distance r increases, the radial wind speed increases approximately linearly, and then decreases with the increase of r after reaching the peak value. In the region of $z = 0.02D - 0.10D$, the wind speed reaches the peak in the radial position $r = 1.0 - 1.5D$ and its value is approximately equal to the initial jet velocity. In the region of $0.1D < z < 0.2D$, the radial wind speed reaches a peak near the radial position $r = 0.75D$ and the peak wind speed is about 75% of the initial jet velocity. With the increase of

altitude, the radial position corresponding to the peak wind speed appears closer to the center of downburst and the decay is faster after reaching the peak value.

3.3 Influence of jet velocity and jet height

In order to investigate the effect of different jet velocities (different Reynolds numbers) on the wind field, three jet velocities were considered: $V_{jet} = 6$ m/s, $V_{jet} = 13$ m/s, $V_{jet} = 20$ m/s, corresponding to Reynolds numbers of 2.5×10^5 , 5.3×10^5 , 8.2×10^5 , respectively, where the jet diameter $D = 610$ mm and jet height $H = 2D$. Fig. 6 compares the normalized vertical profiles of radial wind

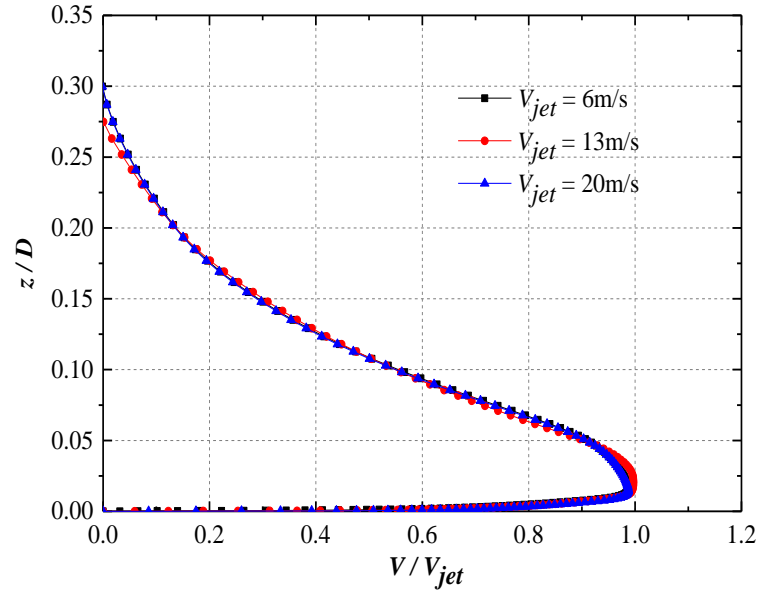


Fig. 6 Influence of jet velocity on vertical profile of radial wind speed at $r = 1.5D$

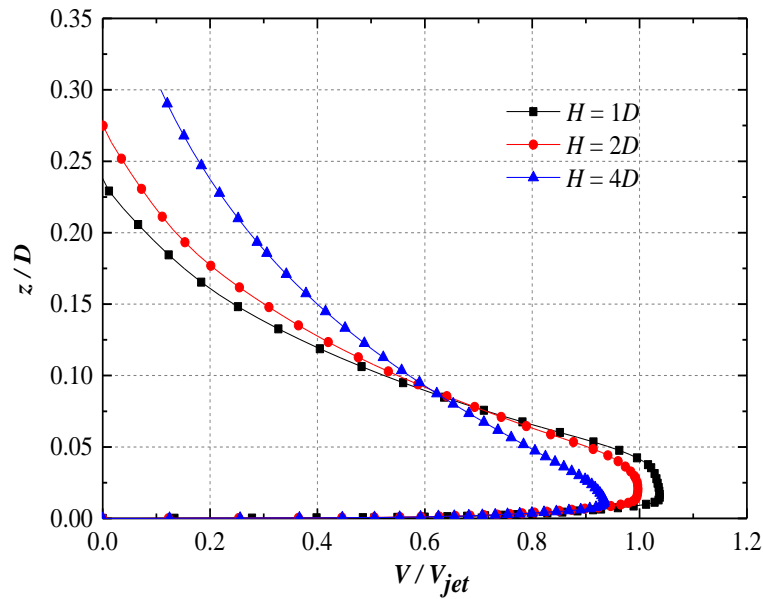


Fig. 7 Influence of jet height on radial wind speed at $r = 1.5D$

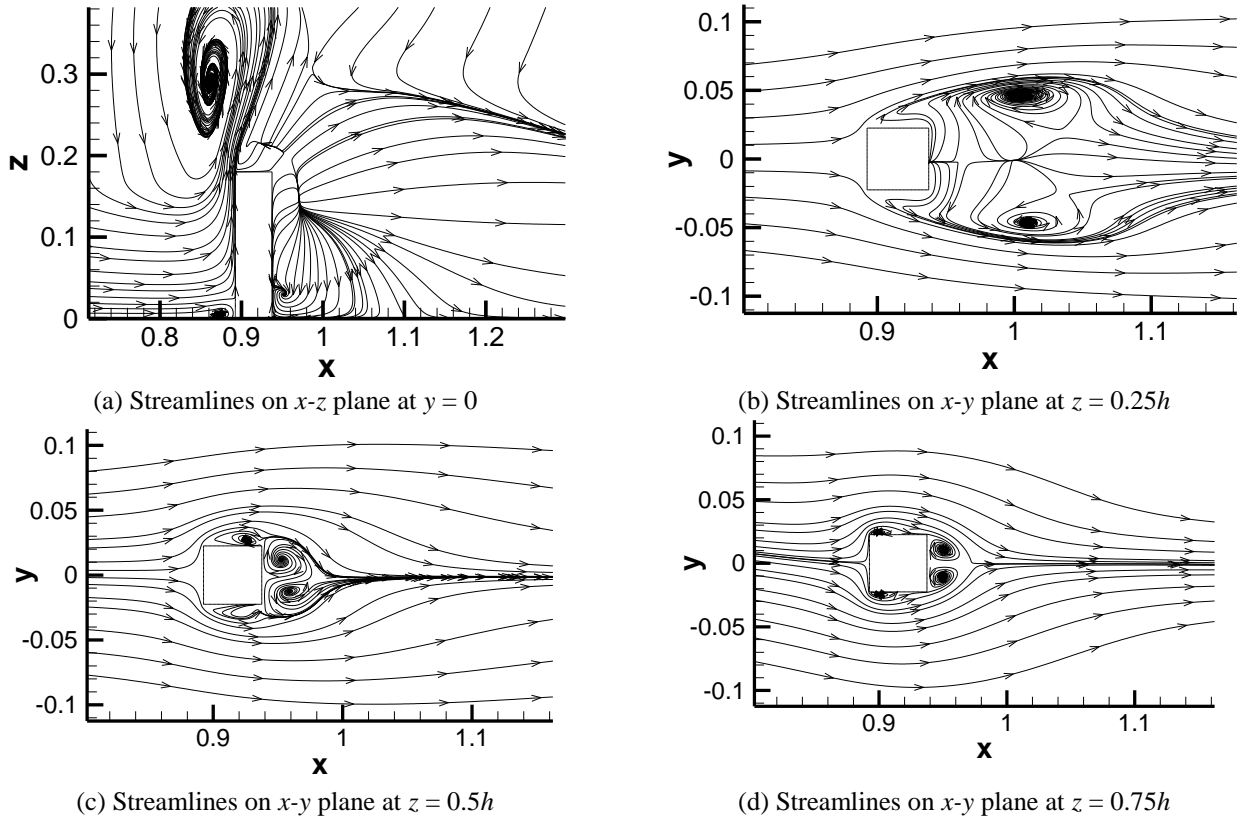
speed at $r = 1.5D$ for three inflow conditions. From Fig. 6, it can be found that the jet velocity has little effect on the normalized vertical profile of radial wind speed. In the range of Reynolds numbers in the present simulation, the characteristics of the downburst wind field change little with Reynolds numbers.

In order to study the effect of the jet heights on the wind field structure, three jet heights $H/D = 1, 2$ and 4 are considered, where the jet velocity $V_{jet} = 13\text{m/s}$ and $D = 610$ mm. The vertical profiles and contours of radial wind speed at $r = 1.5D$ are compared under different jet heights in Fig. 7. It can be found that in the region of $z < 0.1D$, as H/D becomes smaller, the radial wind speed becomes larger. The peak radial wind speeds are $1.04V_{jet}$ and $0.94V_{jet}$ under jet

height $H/D = 1$ and 4 , respectively. It can be explained hereafter. When the flow approaches the wall, there will be more kinetic energy losses under the larger height of the jet. Thus the peak radial wind speed is smaller near the surface. On the other hand, in the region of $z > 0.1D$, as H/D becomes smaller, the radial wind speed becomes smaller at the same height. This is because the horizontal diffusion of the flow decreases in this region when the jet height H becomes smaller.

3.4 Flow structures around high-rise building

Since the wind loads on a high-rise building are closely related to its surrounding flow patterns, it is important to


 Fig. 8 Streamlines around building located at radial position $r=1.5D$

analyze the flow field characteristics around the building. Fig. 8 presents the streamlines around the building located at $r = 1.5D$. It can be seen that flow separation and reattachment occur near the edges and surfaces, and large vortices form in the wake when the high-rise building model is immersed in a downburst wind field, thus affecting its aerodynamics.

Windward face: When a high-rise building is immersed in the conventional atmospheric boundary layer winds, the flow has a stagnation point at a higher elevation ($z = 0.8h - 0.9h$). The flow rises above the stagnation point and crosses the top of the building, and the flow falls downward below that point. In the downburst wind field, it can be seen from Fig. 8(a) that there is a stagnation point at a much lower elevation ($z = 0.1h - 0.2h$). Above the stagnation point, the flow goes upward. In the area below the stagnation point, the flow goes downward, where the energy of the flow is greater, forming a flow reversal. Due to the collision between the reversed flow and the oncoming flow, a vortex forms near the ground finally.

Lateral face: Similar to that in the conventional atmospheric boundary layer, flow separation and reattachment occur near the edges and surfaces of building in the downburst wind field. As shown in Fig. 8(d), flow separates at the leading edge then reattaches at the rear portions of the lateral face at the height $z = 0.75h$. However, as shown in Figs. 8(b) and 8(c), flow separates at the leading edge, but does not reattach at the rear portions at the height $z = 0.25h$ and $z = 0.5h$.

Leeward face: As shown in Figs. 8(c) and 8(d), two vortices which rotate in the opposite direction exist near the leeward of the building at the height $z = 0.5h$ and $z = 0.75h$. At the center of the leeward face, the direction of flow is towards the leeward of the building, that is, the flow reattaches at the center of the leeward and then spreads towards lateral faces. However, as shown in Fig. 8(b), the flow does not reattach at the center of the leeward face at the height $z = 0.25h$.

3.5 Aerodynamic forces

The pressure coefficient distributions and the drag on the high-rise building are analyzed in order to investigate the characteristics of aerodynamic forces. The pressure coefficient C_p on the building surface is defined as follows

$$C_p = \frac{P - P_0}{0.5\rho V_{jet}^2} \quad (6)$$

where P is the pressure; P_0 is mean pressure at jet nozzle; V_{jet} is jet velocity.

The pressure coefficient distributions on the surfaces of the building at the height $z = 0.25h$ are presented with three radial positions, and compared with the experimental results from Zhang *et al.* (2014). Nineteen points are arranged uniformly from the center of the windward face to the center of the leeward face at the height $z = 0.25h$. As shown in Fig. 9, pressure coefficients on the windward face obtained by present numerical simulation and physical

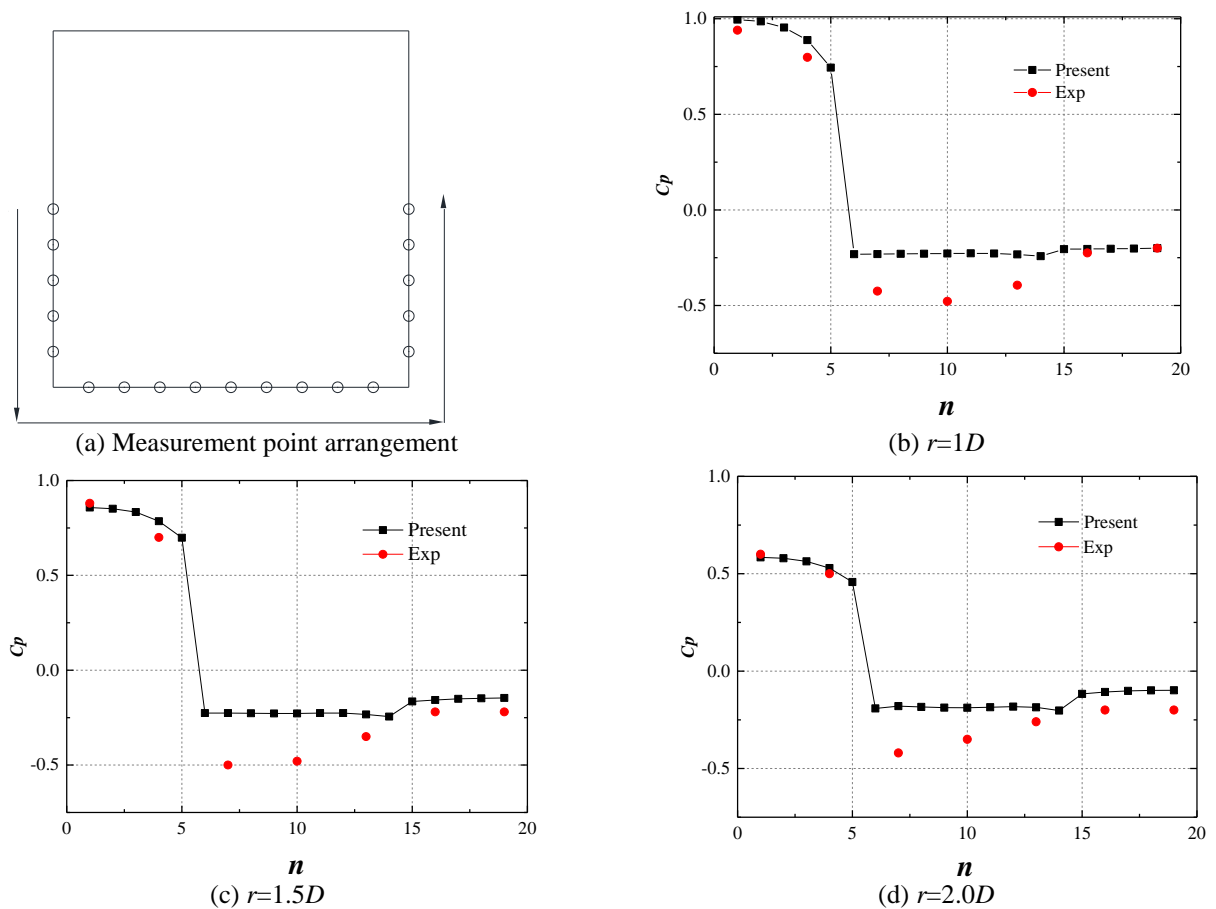


Fig. 9 Measurement point arrangement and comparison of present numerical results with experiments

experiment are consistent. The pressure coefficients on the windward are positive, reaching peak value at the centerline. On the lateral and leeward faces, the pressure coefficients are negative, indicating that suction exists due to the flow separations in these regions. Absolute pressure coefficients on the lateral and leeward faces in present simulation are smaller than that in experimental tests. It may be due to the fact that the numerical simulation is steady, making the vortices on lateral faces weaker. Although some deviations exist on the lateral and leeward faces, the overall trend is basically similar to the experimental results. The effects of downburst on a high-rise building can be numerically simulated with the application of *SST k- ω* turbulence model.

In the remainder of this section, pressure distributions on surfaces of the high-rise building located at the radial position $r = 1.5D$ in the downburst are compared with those in the atmospheric boundary layer, and are investigated by analyzing the surrounding flow structures. Furthermore, pressure distributions on surfaces of the high-rise building located at three radial positions in the downburst wind field are discussed.

Windward face: When the building model is immersed in atmospheric boundary layer winds, the maximum pressure coefficient is found to be at the height about $z = 0.85h$, and the pressure coefficients decrease along the height (e.g., Huang and Chen 2007, Kim and Kanda 2010).

However, when the building model located at radial position $r = 1.5D$ is immersed in the downburst, as shown in Fig. 10(b), the maximum pressure coefficient appears at a much lower elevation ($z = 0.1h - 0.2h$), which is consistent with the height of stagnation point shown in Fig. 8(a). The pressure coefficients decrease along the height, showing an opposite trend compared with that in synoptic atmospheric boundary layer winds.

Fig. 10 compares the distributions of pressure coefficient on the windward face at three radial positions. The maximum pressure coefficient, which is about 1.0, is found to be at a height of $z = 0.25h$ at the radial position $r = 1D$ as shown in Fig. 10(a). As the high-rise building model is moved further away from the downburst center, the maximum pressure coefficient on the windward face decreases since the maximum wind speed decreases with the increase of the distance to the center as shown in Fig. 4. The maximum pressure coefficient decreases to 0.9 at radial position $r = 2.0D$ and the area of $C_p > 0.9$ becomes smaller.

Lateral face: When the building model is immersed in atmospheric boundary layer winds, the absolute value of negative pressure at the leading edge is larger than that at rear portions, and the pressure distributions between upper part and lower part of the lateral face have no significant difference (Kim and Kanda 2010). However, when the building located at radial position $r = 1.5D$ is immersed in

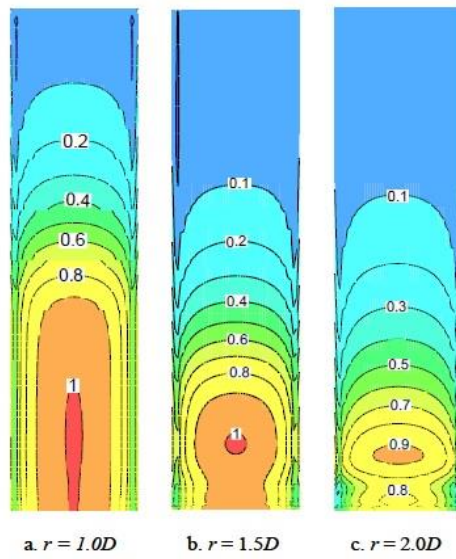


Fig. 10 Windward face pressure coefficient contour

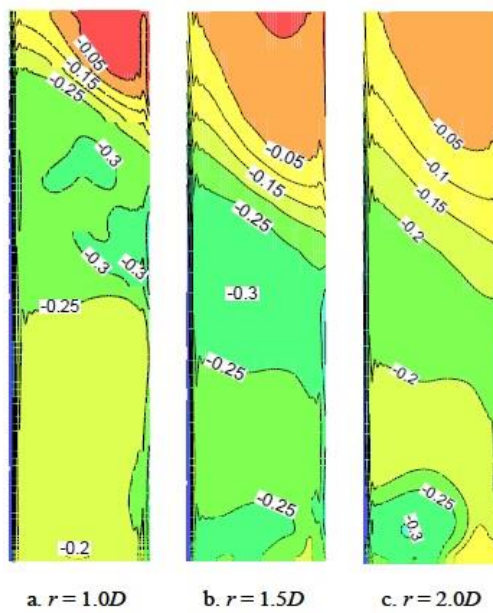


Fig. 11 Lateral face pressure coefficient contour

the downburst, there is a significant difference in the pressure coefficient distributions as shown in Fig. 11(b). The peak pressure coefficient appears near the middle part of the lateral face. At the upper part of lateral face, the absolute value of negative pressure at the leading edge is larger, and recovers towards rear portions. The reason for this phenomenon is that the flow separates at the leading edge and reattaches at the rear portions of the lateral face as shown in Fig. 8(d). However, at the middle and lower part of lateral face, the pressure coefficient distributions are relatively uniform. As shown in Figs. 8(b) and 8(c), the reason for the uniformity is that flow separates at the leading edge, but does not reattach at the rear portions of the lateral face.

Fig. 11 compares the distributions of pressure coefficient on the lateral face at three radial positions. The height of the peak pressure coefficient on the lateral face and its absolute value decrease with the increase of distance to downburst center. When the building is located at the radial position $r = 1D$, the absolute value of peak pressure coefficient is about 0.3 corresponding to a height of $0.65 - 0.70h$. At the radial position $r = 2D$, the peak pressure coefficient is about 0.2, and the height of it decreases to $0.50h$.

Leeward face: The pressure coefficient distributions are relatively uniform in atmospheric boundary layer winds, and large values appear in the surrounding areas (Kim and Kanda 2010). However, when the building located at radial

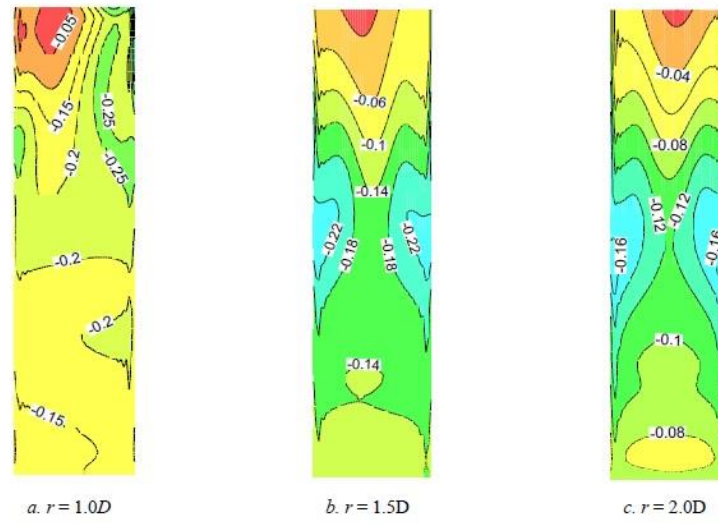


Fig. 12 Leeward face pressure coefficient contour

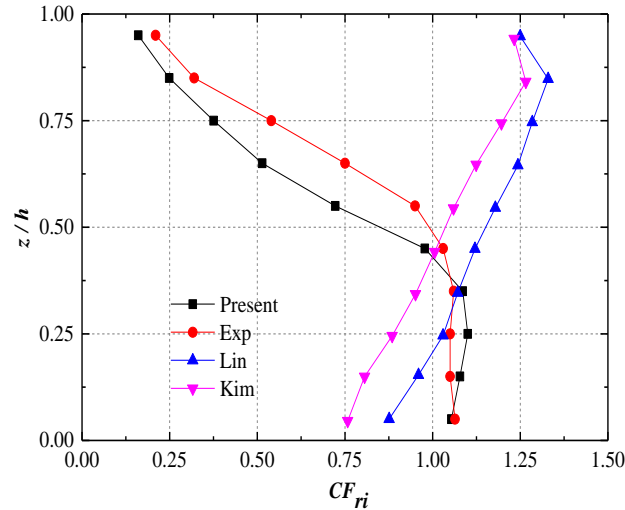


Fig. 13 Variation of drag coefficients with height

position $r = 1.5D$ is immersed in the downburst, pressure coefficients are distributed non-uniformly as shown in Fig. 12(b), and gradually increase towards the edge of the lateral face at the middle and upper parts. This is because the flow reattaches at the center of the upper and middle parts of the leeward face as shown in Figs. 8(c) and 8(d), where the absolute pressure coefficient is relatively smaller. At the lower part of the leeward face, the pressure coefficient distributions are relatively uniform. This uniformity is because the flow does not reattach as shown in Fig. 8(b).

Fig. 12 shows distributions of pressure coefficients on the leeward face at three radial positions. As the high-rise building model is moved further away from the downburst center, the absolute value of the peak pressure coefficient decreases. At the radial position $r = 1.0D$, the absolute value of pressure coefficient at the center of the leeward of the model is 0.2, and it decreases to 0.12 at the radial position $r = 2.0D$.

The high-rise building model is divided into 10 layers uniformly along the height to obtain the drag coefficients CF_{ri} of each layer of the building. CF_{ri} is defined by

$$CF_{ri} = \frac{F_{ri}}{0.5\rho V_{jet}^2 A_i} \quad (7)$$

where F_{ri} is the drag force of i th layer; V_{jet} is jet velocity; A_i is the area of i th layer windward face.

Fig. 13 shows the drag coefficients of each layer of the building located at radial position $r = 1.0D$. The present numerical simulation results are compared with the experimental values from Zhang *et al.* (2014). Good agreement is achieved between the present numerical simulation and the experiment. As shown in Fig. 13, the maximum value of the drag force coefficient from Zhang *et al.* (2014) is 1.05 and the present numerical simulation result is 1.1. The average absolute deviation between

numerical simulation results and measurements is 0.089. This may be due to Reynolds-averaged turbulence model and the steady-state simulation method used in present numerical simulation.

The present numerical results are compared with the previous research (Lin *et al.* 2005, Kim and Kanda 2010) in atmospheric boundary layer winds. The variation of drag coefficients with the height of the building are compared in Fig. 13. It should be noted that the geometry shape of the high-rise building model used in the present study is the same as those used by Lin *et al.* (2005) and Kim and Kanda (2010), the model is a square section with side ratio of 1, aspect ratio of 4. It can be seen from Fig. 13 that in the atmospheric boundary layer winds, the drag coefficients of the high-rise building model increase along the height of the model and reaches a maximum value at the height $z = 0.85h$ (Lin *et al.* 2005, Kim and Kanda 2010). However, the drag coefficient reaches the maximum near the ground in the downburst wind field, and then decreases along the height. This is due to the difference in wind profiles between atmospheric boundary layer winds and downbursts. In the atmospheric boundary layer winds, the upper half of the high-rise building is subjected to the larger along-wind force. However, the lower half of the high-rise building would bear the largest along-wind force in the downburst wind field. Thus, when performing structural design, it is necessary to take into account the wind loading characteristics of high-rise buildings subjected to downburst wind fields, as they are quite different from those of atmospheric boundary layer winds.

4. Conclusions

In the present paper, three dimensional simulations based on the impinging jet model were carried out to investigate the flow field of a steady downburst and its effects on a high-rise building by the *SST k- ω* turbulence model. Some useful conclusions were obtained as follows:

- (1), The steady downburst and its effects on a high-rise building can be numerically simulated with the application of *SST k- ω* turbulence model. In the range of Reynolds numbers studied, the wind field is unaffected by the jet velocity, while the jet height has a significant effect on the wind field.
- (2), In the downburst, at the upper part of the lateral face, the flow separates at the leading edge and then reattaches at the rear portions. At the lower part, the flow separates at the leading edge, but there is no reattachment at the rear portions.
- (3), In the downburst, the maximum pressure coefficient appears at a much lower height of the high-rise building and the pressure coefficient decreases along the height, which shows a different trend compared with those in synoptic atmospheric boundary layer winds. At the upper part of the lateral face, the absolute value of the negative pressure at the leading edge is larger, and recovers towards rear portions due to the special flow characteristics in this region.
- (4), In contrast to that of atmospheric boundary layer winds, the lower half of building bears a the largest along-wind

force. Thus it is necessary in the structural design to take into account the wind load characteristics of high-rise building affected by the downburst.

Acknowledgements

The support by the National Natural Science Foundation of China (Grant Nos. 51720105005, 51578471 and 51708462), and the Fundamental Research Funds for the Central Universities (No.2682016CX006) are greatly acknowledged. Profs. Hui Hu at Iowa State University and Yan Zhang at North Dakota State University are also greatly acknowledged for providing the valuable data.

References

- Aboshosha H., Elawady A., El Ansary A. and El Damatty A. (2016), "Review on dynamic and quasi-static buffeting response of transmission lines under synoptic and non-synoptic winds", *Eng. Struct.*, **112**, 23-46.
- Butler, K., Cao, S., Kareem, A., Tamura, Y. and Ozono, S. (2010), "Surface pressure and wind load characteristics on prisms immersed in a simulated transient gust front flow field", *J. Wind Eng. Ind. Aerod.*, **98**(6), 299-316.
- Chay, M.T. and Letchford, C.W. (2002), "Pressure distributions on a cube in a simulated thunderstorm downburst-Part A: stationary downburst observations", *J. Wind Eng. Ind. Aerod.*, **90**(7), 711-732.
- Choi, E.C.C. (2004), "Field measurement and experimental study of wind speed profile during thunderstorms", *J. Wind Eng. Ind. Aerod.*, **92**(3), 275-290.
- De Gaetano, P., Repetto, M.P., Repetto, T. and Solari, G. (2014), "Separation and classification of extreme wind events from anemometric records", *J. Wind Eng. Ind. Aerod.*, **126**, 132-143.
- Fluent (2005), FLUENT User's Guide, Release 6.2. Fluent Inc., Lebanon, New Hampshire.
- Fujita, T.T. (1985), Report of Projects NIMROD and JAWS. University of Chicago.
- Gast, K.D. and Schroeder, J.L. (2003), "Supercell rear-flank downdraft as sampled in the 2002 thunderstorm outflow experiment", *Proceedings of the 11th Int. Conf. on Wind Eng.*, Lubbock, TX.
- Holmes, J.D. (1999), "Modeling of extreme thunderstorm winds for wind loading of structures and risk assessment", *Wind engineering into the 21st century*, (Eds., A. Larsen, G.L. Larose and F.M. Livesey), Balkema, Rotterdam, The Netherlands, 1409-1415.
- Holmes, J.D. and Oliver, S.E. (2000), "An empirical model of a downburst", *Eng. Struct.*, **22**(9), 1167-1172.
- Huang, G. and Chen, X. (2007), "Wind load effects and equivalent static wind loads of tall buildings based on synchronous pressure measurements", *Eng. Struct.*, **29**(10), 2641-2653.
- Huang, G., Zheng, H., Xu, Y. and Li, Y. (2015), "Spectrum models for nonstationary extreme winds", *J. Struct. Eng.-ASCE*, **141**(10), 04015010.
- Kim, J. and Hangan, H. (2007), "Numerical simulations of impinging jets with application to downbursts", *J. Wind Eng. Ind. Aerod.*, **95**(4), 279-298.
- Kim, Y. and Kanda, J. (2010), "Characteristics of aerodynamic forces and pressures on square plan buildings with height variations", *J. Wind Eng. Ind. Aerod.*, **98**(8), 449-465.
- Lin, N., Letchford, C.W., Tamura, Y., Liang, B. and Nakamura, O. (2005), "Characteristics of wind forces acting on tall buildings",

- J. Wind Eng. Ind. Aerod.*, **93**(3), 217-242.
- Lombardo, F.T., Smith, D.A., Schroeder, J.L. and Mehta, K.C. (2014), "Thunderstorm characteristics of importance to wind engineering", *J. Wind Eng. Ind. Aerod.*, **125**, 121-132.
- Mason, M.S., Wood, G.S. and Fletcher, D.F. (2009), "Numerical simulation of downburst winds", *J. Wind Eng. Ind. Aerod.*, **97**(11), 523-539.
- McConville, A.C., Sterling, M. and Baker, C.J. (2009), "The physical simulation of thunderstorm downbursts using an impinging jet", *Wind Struct.*, **12**(2), 133-149.
- Menter, F.R. (1992), "Performance of popular turbulence model for attached and separated adverse pressure gradient flows", *AIAA J.*, **30**(8), 2066-2072.
- Menter, F.R. (1994), "Two-equation eddy-viscosity turbulence models for engineering applications", *AIAA J.*, **32**(8), 1598-1605.
- Peng, L., Huang, G., Chen, X. and Yang, Q. (2018), "Evolutionary spectra-based time-varying coherence function and application in structural response analysis to downburst winds", *J. Struct. Eng.*, **144**(7), 04018078.
- Selvam, R.P. and Holmes, J.D. (1992), "Numerical simulation of thunderstorm downdrafts", *J. Wind Eng. Ind. Aerod.*, **44**(1-3), 2817-2825.
- Sengupta, A. and Sarkar P.P. (2008), "Experimental measurement and numerical simulation of an impinging jet with application to thunderstorm microburst winds", *J. Wind Eng. Ind. Aerod.*, **96**(3), 345-365.
- Shehata, A.Y., El Damatty, A. and Savory, E. (2005), "Finite element modeling of transmission line under downburst wind loading", *Finite Elem. Anal. Des.*, **42**(1), 71-89.
- Sim, T.S., Ong, M.C., Quek, W.Y., Sum, Z.W., Lai, W.X. and Skote, M. (2016), "A numerical study of microburst-like wind load acting on different block array configurations using an impinging jet model", *J. Fluid. Struct.*, **61**, 184-204.
- Solari, G., De Gaetano, P. and Repetto, M.P. (2015), "Thunderstorm response spectrum: fundamentals and case study", *J. Wind Eng. Ind. Aerod.*, **143**, 62-77.
- Vicroy, D.D. (1991), A simple, analytical, asymmetric microburst model for downdraft estimation, NASA Technical Memorandum 104053.
- Wood, G.S., Kwok, K C.S., Motteram, N.A. and Fletcher, DF. (2001), "Physical and numerical modeling of thunderstorm downbursts", *J. Wind Eng. Ind. Aerod.*, **89**(6), 535-552.
- Xu, Z. and Hangan, H. (2008), "Scale, boundary and inlet condition effects on impinging jets", *J. Wind Eng. Ind. Aerod.*, **96**(12), 2383-2402.
- Yang, Q., Gao, R., Bai, F., Li, T. and Tamura, Y. (2018), "Damage to buildings and structures due to recent devastating wind hazards in East Asia", *Nat. Hazards*, 1-33.
- Zhang, Y., Sarkar, P. and Hu, H. (2014), "An experimental study on wind loads acting on a high-rise building model induced by microburst-like winds", *J. Fluid. Struct.*, **50**, 547-564.